PHYSICAL REVIEW E **96**, 053115 (2017)

Nonlinear and subharmonic stability analysis in film-driven morphological patterns

Matteo Bernard Bertagni* and Carlo Camporeale†
Politecnico di Torino, DIATI, Corso Duca degli Abruzzi, 24, 10129 Torino, Italy

(Received 18 January 2017; revised manuscript received 24 May 2017; published 27 November 2017)

The interaction of a gravity-driven water film with an evolving solid substrate (calcite or ice) results in the formation of fascinating wavy patterns similar both in caves and in ice-falls. Due to their remarkable similarity, we adopt a unified approach in the study of pattern formation of longitudinally oriented organ-pipe-like structures, called flutings. Since the morphogenesis of cave patterns can evolve for millennia, they have an additional value as silent repositories of past climates. Fluting formation is studied with the aid of gradient expansion and center manifold projection. In particular, through gradient expansion, a Benney-type equation accounting for the movable boundary is obtained. The coupling with a wall evolution equation provides a morphodynamic model for fluting formation, explored through linear and nonlinear analyses. In this way, closed relationships for the selected wave number and for the finite amplitude are achieved. However, as finite-amplitude monochromatic waves may be destabilized by nonlinear interactions with other modes, we verify, through center manifold projection, the stability of the fundamental to subharmonic disturbances. Conclusively, we perform numerical simulations of the fully nonlinear equations to validate the theory results.

DOI: 10.1103/PhysRevE.96.053115

I. INTRODUCTION

Pattern formations carved by water in ice or stones are ubiquitous in nature and their beauty attracts the curiosity of scientists and common people alike. A plethora of fluid dynamic-driven forms arises as spatial instabilities, triggered by nonlinear interactions between an open channel flow and a movable boundary. This work considers the effect of a thin film running over ice or calcite substrate.

In the context of cave environments, precipitation-dissolution processes concur to shape different types of speleothems, which are karst formations typically generated in limestone or dolostone solutional caves [1]. Since their morphogenesis can last thousands of years, they are silent repositories of past climates. For this reason, their importance as a palaeoclimate proxy is growing among geologists [2] and the development of advanced quantitative models that link patterns to hydrology is becoming compelling. Although the hydrogeochemical aspects of cave speleogenesis are well-known, a mathematical approach to the morphodynamic modeling of these water-driven patterns has been studied only recently, for example, in the case of stalactite formation or subcentimeter ripples on their surface [3,4].

Through a remarkable parallelism, the ice environment is able to generate very similar patterns which are driven by melting-freezing processes, again regulated by the interaction with thin water films. Also in this case, some analytical and experimental works have been performed on ice-ripples [5,6], on supraglacial channel formation [7], and on ripple formation over the surface of icicles [8–10].

Figure 1 shows two pictures and a sketch of the geometrical framework regarding the target of the present work, that is the formation of longitudinally oriented organ-pipe-like structures, called flutings, which are widespread in caves and ice-falls. Flutings are due to a gravity-driven thin film flowing over an inclined (usually overhung) plane, composed of stone or ice. In the cave case, the underlying process is the precipitation-dissolution of calcite content dissolved in the water film, while in the ice case the freezing-melting condition is determined by a heat flux balance at the liquid-solid interface. Although the driving mechanism is different in the two environments, a previous work has shown that a unified approach is possible [11], since at *inverted conditions* ($\theta > \pi/2$, where θ is the angle with the horizontal) the key role in driving the morphogenesis is played by the free surface dynamics.

In the present paper, the classical long-wave theory for falling films leads to a Benney-type equation that represents a novelty in the morphodynamic context. In fact, from the seminal work of Ref. [12], the Benney equation has been broadly analyzed [13–15], improved [16,17], and extended to its weakly nonlinear version [18–20]. However, to the authors' knowledge, a Benney-type equation accounting also for an evolving solid substrate has never been achieved. Partial exception can be found in Refs. [21,22], where a thin flexible inclined boundary wall is considered, and in Refs. [23,24], where the interaction of liquid droplets with dissolving substrate is analyzed. The coupling of our Benney-type equation with a wall evolution equation provides an algebraic eigenvalue problem considerably simplified, but in complete agreement, with respect to the outcomes of the previous work [11]. Namely, flutings are long-wave instabilities that develop at inverted conditions for all Reynolds numbers. This simplification furnishes a more suitable form for the eigenfunctions and therefore allows one to analytically investigate the problem nonlinearly for the first time. To this aim, a weakly nonlinear analysis is addressed through the method of the center manifold projection.

The use of the center manifold theorem permits the stable modes to be projected onto the unstable ones, thus obtaining an amplitude differential equations with only unstable modes involved. By considering only the fundamental as the unstable mode, the celebrated Stuart-Landau equation for the amplitude dynamics is provided and, consequently, a solution for

---

*matteo.bertagni@polito.it
†carlo.camporeale@polito.it

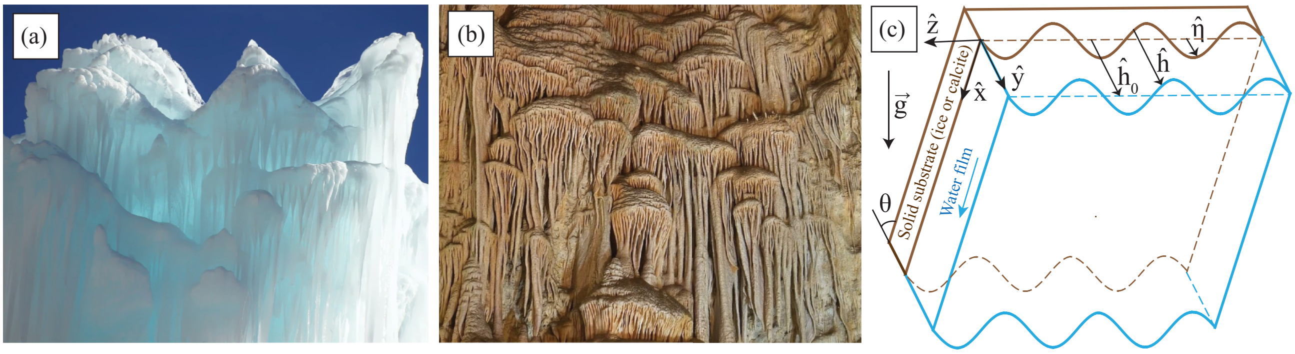

FIG. 1. (a) Example of ice flutings, photo courtesy of Antonio Giani. (b) Flowstone with cave flutings, photo courtesy of Alexey Sergeev. (c) Sketch of the water film flowing down the solid substrate.

the finite amplitude is given in a closed form. As far as the karst patterns are concerned, an explicit relation between the geomorphic features (wavelength and amplitude) and the flow parameters (Reynolds number, calcium content, etc.) is a step forward for definition of pattern-based palaeoreconstructive proxies.

Furthermore, the nonlinear analysis highlights additional issues. Formally, the sum of the linear and nonlinear solutions define in a complete way the spatial structure of flutings in the parameter space. Nevertheless, finite-amplitude monochromatic waves may be destabilized by modes with different wavenumbers. In experimental and theoretical works on falling liquid films [25–27], sideband and subharmonic instability were detected. Subharmonic instability was also found in other open-flow systems with long-wave instabilities [28–30]. However, we point out that differently from these last works, in our system the modulation is not parallel to the base flow, but it is transversal to it; see Fig. 1(c). For these reasons, we have performed a subharmonic stability analysis, showing that, even though the subharmonic of the fundamental is linearly unstable, the rising effect of the nonlinearities may allow the fundamental to saturate and the subharmonic to decay. From a practical point of view, this means that the predictions of the linear and nonlinear analyses are robust.

Finally, we perform numerical simulations of the full equations. The wavelength selection accurately confirms the linear theory. Furthermore, the nonlinear behavior of the hydrodynamic quantity, that is the key element in the instability, is correctly captured by the center manifold projection. Indeed in the phase space, hydrodynamics is mainly described by the center manifold, so finite-amplitude prediction and nonlinear stability of the film depth perturbation are well verified. The same outcome does not hold for the saturated value of the morphological quantity, since this is primarily connected to the stable manifold. Nevertheless, an exact analytical relation for flutings finite amplitude is given for the ice environment through the wall evolution equation. While the saturation of the cave pattern is not reached as the calcium-carbonate deposits endlessly. This may explain the very large amplitude of flutings in many karst environments worldwide; see Fig. 7.

The paper is organized as follows: in Sec. II the mathematical problem is formulated for both types of patterns, ice and karst flutings; in Sec. III the linear analysis is performed and an explicit form of the selected wavelength of the fundamental is given; in Sec. IV the Stuart-Landau equation for finite amplitude of flutings is achieved through the center-unstable manifold technique. Then, the stability of the finite-amplitude to subharmonic disturbances is verified both analytically and numerically. Finally, the outcomes of the numerical simulations of the full equations are provided. Section V presents a discussion of the results.

II. MATHEMATICAL MODEL

A. Water film dynamics through long-wave theory

The dynamical system leading to fluting formation consists in a water film flowing over an overhanging evolving solid substrate (calcite or ice), as presented in the sketch of Fig. 1(c). The unperturbed solution for the water film provides the well-known Nusselt's semi-parabolic velocity profile [31], whose solutions in terms of film thickness $\hat{h}_0$ and surface velocity $\hat{u}_0$ are

$$\hat{h}_0 = \left(\frac{3\,\nu\,\hat{Q}}{g\,\sin\theta}\right)^{1/3} \qquad \hat{u}_0 = \left(\frac{9\,g\,\hat{Q}^2\,\sin\theta}{8\,\nu}\right)^{1/3}, \tag{1}$$

where ν is the kinematic viscosity, g the gravitational acceleration, θ the angle with the horizontal, and $\hat{Q} = 2\hat{u}_0\hat{h}_0/3$ the flow rate per unit span.. The hat refers to dimensional variables. Flutings usually develop with very low Reynolds numbers ($R = \hat{h}_0\hat{u}_0/\nu \ll 1$), a slope of the interface not too far from verticality and small ratio ϵ between the film thickness and the pattern wavelength (order 10^{-3}), so that they can be regarded as long-wave instabilities. This is especially so when the effect of surface tension is predominant with respect to viscous stresses, i.e., low values of the capillary number $\mathrm{Ca} = \mu\hat{u}_0/\sigma$, σ and μ being the surface tension and the dynamic viscosity of water, respectively. In the case of a film flowing over a fixed flat boundary, the long-wave approach through the so-called gradient expansion [32] leads to the well-known Benney equation [12] and its weakly nonlinear versions (Kuramoto-Sivashinsky equation) [18–20]; see Ref. [33] for a complete review. In the present morphodynamic context, the gradient expansion technique needs to be extended to the case where the lower boundary is also unknown and deformable (see also Ref. [34] for a recent application in the crenulation instability problem). Let us adopt Nusselt's solutions to make dimensionless lengths, velocities, pressure, and time, respectively: ($\hat{h}_0$, $\hat{u}_0$, $\rho\hat{u}_0^2$, $\hat{h}_0/\hat{u}_0$). Accordingly, (x,

y, z) are defined as the dimensionless downslope, normal-to-the unperturbed solid surface and span-wise directions, respectively [see Fig. 1(c)]; $\mathbf{u}=(u,v,w)$ are the corresponding velocities and p stays for pressure. The elevations $y=\eta(x,z,t)$ and $y=\eta(x,z,t)+h(x,z,t)$ correspond to the liquid-solid interface and the free surface, respectively. After introducing a gradient expansion transformation of the type $(\partial_x,\partial_z,\partial_t,v)\to\varepsilon(\partial_x,\partial_z,\partial_t,v)$, the Navier-Stokes equations, truncated at order ϵ, read

$$\nabla\cdot\mathbf{u}=0, \tag{2}$$

$$\varepsilon R(u_t+\mathbf{u}\cdot\nabla u)+\varepsilon R\, p_x-u_{yy}-2=O(\epsilon^2), \tag{3}$$

$$R\, p_y-\varepsilon v_{yy}+\delta=O(\epsilon^2), \tag{4}$$

$$\varepsilon R(w_t+\mathbf{u}\cdot\nabla w)+\varepsilon R p_z-w_{yy}=O(\epsilon^2), \tag{5}$$

where subscripts refer to the partial derivatives and $\delta=2\cot\theta$. Notice that for fluting formation, i.e., $R\ll 1$, the convective terms in Eqs. (3)–(5) could be neglected. In Sec. III A we show why it is instead important to keep these terms. On the liquid-solid interface, no slip and the dynamic condition are

$$u=w=0,\quad v=\eta_t, \tag{6}$$

while on the free surface, the boundary conditions read

$$(h+\eta)_t=-v+u(h+\eta)_x+w(h+\eta)_z, \tag{7}$$

$$R\, p+2\varepsilon\partial_y v=-\mathcal{C}[(h+\eta)_{xx}+(h+\eta)_{zz}], \tag{8}$$

$$u_y=w_y=0, \tag{9}$$

where $\mathcal{C}$ is an inverse capillary number, i.e., $\mathcal{C}=1/Ca$. Equations (8) and (9) define the dynamic conditions, whereas Eq. (7) is the kinematic condition, which will be used later on as a solvability equation. Carrying out the long wave approach, the variables are expanded in powers of ϵ: $(u,v,w,p)=(u_0,v_0,w_0,p_0)+\epsilon(u_1,v_1,w_1,p_1)+O(\epsilon^2)$. Moreover, $\mathcal{C}R^{-1}$ is considered of order ϵ^{-2}, to assure the validity of the boundary layer approximation and in agreement with experimental observations [32] (e.g., $R\sim 10^{-2}$ and $\theta=\pi/2+\pi/10$ give $\mathcal{C}\sim 10^4$).

Substituting the gradient expansion in the hydrodynamic problem Eqs. (2)–(9), and collecting coefficients of like powers of ϵ, we obtain the problems at the different orders. At the leading order, the system reduces to

$$u_{0,yy}=-2,\quad w_0=0,\quad v_{0,y}+u_{0,x}=0, \tag{10}$$

$$p_{0,y}=-\delta/R,\quad u_0|_\eta=0,\quad u_{0,y}|_{\eta+h}=0, \tag{11}$$

$$v_0|_\eta=\eta_t,\quad p_0|_{\eta+h}=-\mathcal{C}R^{-1}[(h+\eta)_{xx}+(h+\eta)_{zz}], \tag{12}$$

with solutions

$$u_0=(y-\eta)(2h-y+\eta), \tag{13}$$

$$v_0=\eta_t-(y-\eta)[h_x(y-\eta)+\eta_x(-2h-\eta+y)], \tag{14}$$

$$w_0=0, \tag{15}$$

$$p_0=R^{-1}\{\delta(h+\eta-y)-\mathcal{C}[(h+\eta)_{zz}+(h+\eta)_{xx}]\}. \tag{16}$$

At the order ϵ, the system reads

$$R\, u_{0,t}+R(p_{0,x}+u_0u_{0,x}+v_0u_{0,y})=u_{1,yy}, \tag{17}$$

$$Rp_{0,z}=w_{1,yy},\quad u_{1,x}+v_{1,y}+w_{1,z}=0, \tag{18}$$

$$u_1|_\eta=0,\quad u_{1,y}|_{h+\eta}=0,\quad w_1|_\eta=0, \tag{19}$$

$$w_{1,y}|_{h+\eta}=0,\quad v_1|_\eta=0, \tag{20}$$

whose solutions are cumbersome and reported in the Appendix A for the sake of space. The solutions obtained for the flow field can now be substituted into the kinematic condition Eq. (7), which serves as solvability equation. To order ϵ, this leads to the first main equation of our analysis:

$$h_t+2h^2h_x+\frac{8}{15}Rh^5\left(6h_x^2+h_{xx}h\right)++\nabla_{xz}\cdot\left[-\delta\frac{h^3}{3}\nabla_{xz}(h+\eta)+\mathcal{C}\frac{h^3}{3}\nabla_{xz}\nabla^2_{xz}(h+\eta)\right]=0. \tag{21}$$

The topic of a falling film flowing on a nonrigid wall has been previously investigated in Refs. [21,22]. However, both works consider a thin flexible inclined wall and furnish two coupled equations for the free surface and wall dynamics. Instead, Eq. (21) is the first Benney-type equation accounting for an evolving solid substrate. If one fixes the bottom to be undeformable, namely $\eta=0$, Eq. (21) reduces to the standard Benney equation [12], with the effect of surface tension as firstly introduced in Ref. [35].

B. Wall evolution equation

To address the morphological instability, a second equation, uniquely for the wall evolution, is necessary. We first consider the ice environment, where the heat propagation determines melting-freezing processes at the interface. The disequilibrium in the heat fluxes is regulated by the so-called Stefan's equation,

$$\rho_i\lambda_f\,\hat\eta_{\hat t}=[(\kappa_i\nabla\hat T_i)_{LS^-}-(\kappa_w\nabla\hat T_w)_{LS^+}]\cdot\mathbf{n}_{LS}, \tag{22}$$

where $\kappa_{i,w}$ and $\hat T_{w,i}$ are the thermal conductivity and the temperature for water and ice, respectively, ρ_i is the ice density, λ_f the latent heat, $\mathbf{n}_{\mathrm{LS}}$ the normal versor to the liquid-solid interface LS. We now briefly summarize the derivation of a more amenable form for Eq. (22), following Ref. [11]. At first, the temperature can be decomposed into the sum of a base state plus a small pattern-induced perturbation $\hat T_{w,i}=\hat T^0_{w,i}(\hat z)+\zeta\,\hat\Theta_{w,i}(\hat x,\hat y,\hat z)$. Then, another normalized coordinate is introduced $\xi_i=(\hat y-\hat\eta)/(\hat b+\hat\eta)$ to rectangularize also the solid domain, $\hat b$ being an assigned depth in the ice. Hence, both liquid and solid domains are rectangularized, $\xi_w\in[0,1]$ and $\xi_i\in[-1,0]$, respectively. In this way, the base state for the temperature is linearly distributed over the depth,

$$\hat{T}_w^0 = \hat{T}_f \xi_w, \quad \hat{T}_i^0 = \hat{T}_b \xi_i, \tag{23}$$

where $\hat{T}_{f,b}$ are the temperature at the free surface and at $\hat{y} = -\hat{b}$, respectively. Due to the very low Reynolds numbers, thermal convection can be neglected in the heat equation for the liquid phase. Thus, $\hat{T}$ satisfies the Laplace equation $\nabla^2 \hat{T} = 0$ in both domains. Using the normalized coordinates and Fourier-transforming from $(\hat{x}, \hat{z})$ to the horizontal wave numbers $(\hat{\alpha}, \hat{k})$, the diffusive thermal problem at first order in ζ becomes

$$\hat{\Theta}^*_{w,\xi\xi} - \hat{h}_0^2 \hat{K}^2 \hat{\Theta}^*_w + \hat{h}_0 \hat{K}^2 \hat{T}_f (\hat{\eta}_1^* + \xi_w \hat{h}_1^*) = 0, \tag{24}$$

$$\hat{\Theta}^*_{i,\xi\xi} - \hat{b}^2 \hat{K}^2 \hat{\Theta}^*_i + \hat{\eta}_1^* \hat{b} \hat{K}^2 \hat{T}_b (1 + \xi_i) = 0, \tag{25}$$

where the asterisk refers to the Fourier transform, $\hat{K}^2 = \hat{\alpha}^2 + \hat{k}^2$ and $\hat{h}$ and $\hat{\eta}$ have been decomposed into the sum of a basic state and a small local perturbation, i.e., $\hat{h} = \hat{h}_0 + \zeta \hat{h}_1$ and $\hat{\eta} = \hat{\eta}_0 + \zeta \hat{\eta}_1$. The boundary conditions for Eqs. (24) and (25) ensure melting temperature at the liquid-solid interface and continuity of the heat flux throughout the domain,

$$\hat{\Theta}^*_w = \hat{\Theta}^*_i = \hat{\Theta}^*_{w,\xi}|_{\xi_w = 1} = \hat{\Theta}^*_{i,\xi}|_{\xi_i = -1} = 0. \tag{26}$$

Solving the problems Eqs. (24)–(26) and substituting in Eq. (22), at first order in ζ, yields

$$\rho_i \lambda_f (\hat{\eta}_0 + \zeta \hat{\eta}_1)_{\hat{t}} = \hat{I}_i - \hat{I}_w + \zeta \left(\frac{\hat{h}_1}{\hat{h}_0} \hat{I}_w - \frac{\hat{\eta}_1}{\hat{b}} \hat{I}_i - \frac{\hat{K}^2}{2} \mathcal{P} \right), \tag{27}$$

where $\mathcal{P} = [(2\hat{\eta}_1 + \hat{h}_1)\kappa_w \hat{T}_f + \hat{\eta}_1 \kappa_i \hat{T}_b]$, $\hat{I}_i = \kappa_i \hat{T}_b / \hat{b}$, $\hat{I}_w = \kappa_w \hat{T}_f / \hat{h}_0$. The third term in the brackets of Eq. (27) is a diffusive term whose numerical influence we have verified being negligible. Without considering the perturbations, the liquid-solid interface rigidly translates due to a freezing/melting process. Both experimentally and in field observation, measuring a uniform vertical translation of the interface might be a simpler task than evaluating the temperature at an assigned depth in the ice [36]. Thus, for assigned values of the air temperature, the ice depth and the translation rate, $\hat{\eta}_0 = \hat{V}_I \hat{t}$, from Eq. (27) it follows

$$\hat{T}_b = (\rho_i \lambda_f \hat{V}_I + \hat{I}_w) \frac{\hat{b}}{\kappa_i}. \tag{28}$$

Notice that $\hat{T}_b$ is defined as positive to have a negative temperature at $\hat{y} = -\hat{b}$; see Eq. (23). Substituting Eq. (28) in Eq. (27) yields

$$\hat{\eta}_t = \hat{V}_I + (\hat{h} - \hat{h}_0)\hat{B}_I - (\hat{\eta} - \hat{V}_I \hat{t})\hat{B}_I / r, \tag{29}$$

where $\hat{B}_I = \hat{I}_w / (\rho_i \lambda_f \hat{h}_0)$, $r = \hat{b}/\hat{h}_0$ and $\hat{V}_I \ll \hat{B}_I \hat{h}_0$.

In the karst context, the precipitation-dissolution processes of calcium carbonate are able to shape multitudinous speleothems. In particular, the evolution of the liquid-solid interface is driven by reactions that can be stoichiometrically summarized as [37]

$$CaCO_3 + CO_2 + H_2O \rightleftharpoons Ca^{++} + 2HCO_3^-. \tag{30}$$

From Eq. (30), one can notice that for each molecule of $CaCO_3$ depositing on the solid surface, there is a molecule of CO_2 diffusing into the atmosphere. This is the key principle of the equation derived by Ref. [3], as briefly summarized below. Let us start from the slowest chemical reactions involved in the growth of speleothems, which are those coupling carbon dioxide to bicarbonate,

$$CO_2 + H_2O \overset{k_{\pm 1}}{\rightleftharpoons} H^+ + HCO_3^-, \tag{31}$$

$$CO_2 + OH^- \overset{k_{\pm 2}}{\rightleftharpoons} HCO_3^-. \tag{32}$$

From Eqs. (31) and (32), the production rate of CO_2 can be written as

$$R_{CO_2} = k_-[HCO_3^-] - k_+[CO_2], \tag{33}$$

where the square brackets refer to concentrations and

$$k_- = k_{-1}[H^+] + k_{-2}, \quad k_+ = k_{+1} + k_{+2}[OH^-]. \tag{34}$$

To evaluate carbon dioxide dynamics, a full reaction-diffusion equation for $[CO_2]$ within the fluid layer is considered. Then, some assumptions are introduced: (i) the concentrations of the other chemical species are almost constant over the film, (ii) the longitudinal and transversal diffusion and advection of CO_2 are negligible, (iii) $[CO_2] = \mathcal{H} C_\infty (1 + \phi(x, \xi, z, t))$, where $\mathcal{H}$ is Henry's constant, C_∞ is the far atmospheric carbon dioxide concentration, and ξ is the normalized coordinate that rectangularizes the fluid domain, i.e., $\xi = (\hat{y} - \hat{\eta})/\hat{h}$. In these conditions, the dimensionless reaction-diffusion equation for $[CO_2]$ reads

$$\phi_{\xi\xi} = h^2 \Delta (\phi - \mathcal{U}), \tag{35}$$

where

$$\Delta = \frac{k_+ \hat{h}_0^2}{D_w}, \quad \mathcal{U} = \frac{k_-[HCO_3^-]}{k_+ \mathcal{H} C_\infty} - 1, \tag{36}$$

D_w being the carbon dioxide diffusivity in water. The two boundary conditions for Eq. (35) ensure zero flux of carbon dioxide at the solid interface and flux continuity between the fluid and the atmosphere. Because of the latter condition, the solution of Eq. (35) depends on the atmospheric carbon dioxide field C_a, that satisfies the Laplace equation. In cylindrical coordinates, it reads $C_a = C_\infty + A/\hat{r}$ being $\hat{r}$ the dimensional distance from the center of the stalactite. Although in our case the base state geometry is planar, in Ref. [3] it was demonstrated the irrelevance of the geometry considered to the final result. For this reason, as done in Ref. [3], the more amenable cylindrical coordinates for the Laplace equation are adopted. It follows that

$$\phi|_{\xi=1} = \frac{A}{\hat{R}_s C_\infty}, \quad \hat{\mathcal{F}} = \frac{D_a A}{\hat{R}_s^2} = -\frac{D_w \mathcal{H} C_\infty}{\hat{R}_s} \phi_\xi|_{\xi=1}, \tag{37}$$

where $\hat{R}_s$ represents the radius of the stalactite ($\hat{R}_s \gg \hat{h}$), $\hat{\mathcal{F}}$ is the dimensional flux of carbon dioxide leaving the film into the atmosphere (calculated through Fick law) and D_a is the diffusivity of CO_2 in air. Eliminating the constant A from Eq. (37), the two boundary conditions are eventually achieved,

$$\phi_\xi|_{\xi=0} = 0, \quad \phi_\xi|_{\xi=1} = -\frac{\hat h D_a}{\hat R_s \mathcal{H} D_w}\phi|_{\xi=1}. \tag{38}$$

Recalling that $\Delta \ll 1$, a solution of the problem Eqs. (35)–(38) to the lowest order in Δ reads

$$\phi = \Delta \hat h^2 \mathcal{U}\left(\frac{1-\xi^2}{2} + \frac{\mathcal{H} D_w \hat R_s}{D_a \hat h}\right). \tag{39}$$

At this point, it is sufficient to equal the total flux of CO_2 leaving the fluid by the free surface to the total flux of $CaCO_3$ depositing on the solid wall. The result reads

$$\hat{\mathcal{F}}_{\mathrm{CaCO_3}} = \varrho\, \hat\eta_{\hat t} = \hat h(k_-[\mathrm{HCO_3^-}] - k_+ \mathcal{H} C_\infty), \tag{40}$$

where ϱ is the ratio of molar mass to density of calcite. Due to the assumptions previously made, the whole content of the brackets in Eq. (40), denoted as $\varrho \hat B_K$, can be considered independent of hydrodynamics. Thus, Eq. (40) reduces to

$$\hat\eta_{\hat t} = \hat h \hat B_K. \tag{41}$$

Similar to the ice case, even in not-perturbed conditions the liquid-solid interface undergoes a vertical translation ($\hat V_K = \hat h_0 \hat B_K$) due the precipitation of $CaCO_3$ contained in the liquid film.

Eventually, the corresponding dimensionless evolution equations of Eqs. (29)–(41) read

$$\eta_t = V_I + (h-1)/\gamma_I - (\eta - V_I t)/(\gamma_I\, r) \qquad \text{Ice}, \tag{42a}$$

$$\eta_t = V_K + (h-1)/\gamma_K \qquad \text{Karst}, \tag{42b}$$

where $\gamma_{I,K} = \hat u_0/(B_{I,K}\hat h_0)$ is the ratio of the morphological to hydrodynamic time scale. The equations become equivalent for $\hat b \to \infty$ and consequently $r \to \infty$ Assuming $\hat T_s = 0.01\,^\circ\mathrm{C}$, $\hat b = 0.5$ m, $\hat V_I = 4$ cm/d for the ice case and standard conditions for speleothem formation [3] one obtains

$$\gamma_I \sim 10^4 R, \quad \gamma_K = \frac{\hat u_0}{\hat c}, \tag{43}$$

where $\hat c$ is the average velocity of speleothem formation (henceforth $\hat c = 5$ cm/century). Equations (43) furnish γ_I of order 10^2 and γ_K of order 10^7 or larger. In fact, karst flutings evolve much slower than their ice counterpart. To sum up, the dimensionless differential system for fluting formation is provided by the two equations accounting for the free surface and bottom evolution, namely Eqs. (21) and (42).

III. LINEAR ANALYSIS OF FLUTING FORMATION

A. 2D analysis

With the aim of addressing a linear stability analysis, a normal mode ansatz is set in the form

$$(h,\eta) = (1, V_{I,K} t) + \zeta(H,\Lambda) e^{i\alpha x + ikz + \lambda t}, \tag{44}$$

where α and k are the longitudinal and transversal wave numbers, respectively; the real part of λ determines the growth rate, while its imaginary part stays for the angular phase. By substituting Eq. (44) into Eqs. (21) and (42) and linearizing we obtain

$$\mathbf{L}_{I,K}\begin{pmatrix} H \\ \Lambda \end{pmatrix} = 0, \tag{45}$$

where the matrices $\mathbf{L}_{I,K}$ are reported in the Appendix B. After imposing the determinant of the matrices equal to zero, the dispersion relation are obtained,

$$f_{I,K}(\lambda,\alpha,k,\delta,\gamma,R,\mathcal{C}) = 0, \tag{46}$$

whose solutions $\lambda_{1,2}$ are the corresponding eigenvalues of the algebraic linear system Eq. (45). Both f and the eigenvalues $\lambda_{1,2}$ are reported in Appendix B for the karst and the ice cases. Although the two problems are slightly different due to Eqs. (42), the same considerations hold for both environments. This is due to the fact that the dynamics is driven by the hydrodynamics [11].

The control parameters in the system are apparently three: δ, R and $\mathcal{C}$. However, through the definition of the capillary number and Eqs. (1), $\mathcal{C}$ can be recast in a form involving its dependence on δ and R, as done for example in Ref. [38]. This leads to

$$\mathcal{C} = \frac{\mathrm{Ka}}{(\sin\theta R^2)^{1/3}}, \tag{47}$$

where $\mathrm{Ka} = \sigma/(\rho g^{1/3}\nu^{4/3})$ is the Kapitza number, that depends only on the fluid properties and it is thus constant for our purpose. Equation (47) reduces the effective control parameters to two: R and δ. Fixing an overhanging wall, one may evaluate the eigenvalues behaviours with respect to different values of R.

Figure 2 shows the growth rate λ_2^r in the wave numbers plane (while λ_1^r is always negative). For sufficiently small R, the absolute maximum of λ_2^r lays on the k axis ($\alpha = 0$), panel a_1. Therefore, the fastest-growing mode is associated with a transverse perturbation, i.e., flutings. There is also a relative maximum on the α axis, but its value is smaller, as reported in panel a_2. Instead, increasing R, the longitudinal maximum on the α axis ($k = 0$) exceeds the transverse one, see panels b_1 and b_2. In addition, in panel b_2 it is also furnished λ_2^r under the Stokes approximation (red dotted line). Due to the relatively high values of R, the lack of the convective terms jeopardizes the correct boundary of the ripple-fluting transition. Instead in panel a_2, where R is smaller, the computation of λ_2^r is less affected by the Stokes approximation. Hence, although fluting formation could be modelled using the Stokes approximation, it would be impossible to correctly define the margin between the fluting and ripple regimes.

To differentiate these two regimes, the transition Reynolds number R_t below which flutings develop is evaluated with respect to the deviation from the vertical $\theta - \pi/2$ (Fig. 3). It turns out that it is $O(10^{-1})$ for the ice case and $O(10^{-2})$ for the karst case.

Overall, for fluting formation ($R < R_t$), we can consider only the span-wise perturbation and thus develop a more parsimonious model.

B. 1D analysis

The previous section has demonstrated that for low Reynolds numbers, i.e., $R < R_t$, the fastest growing mode

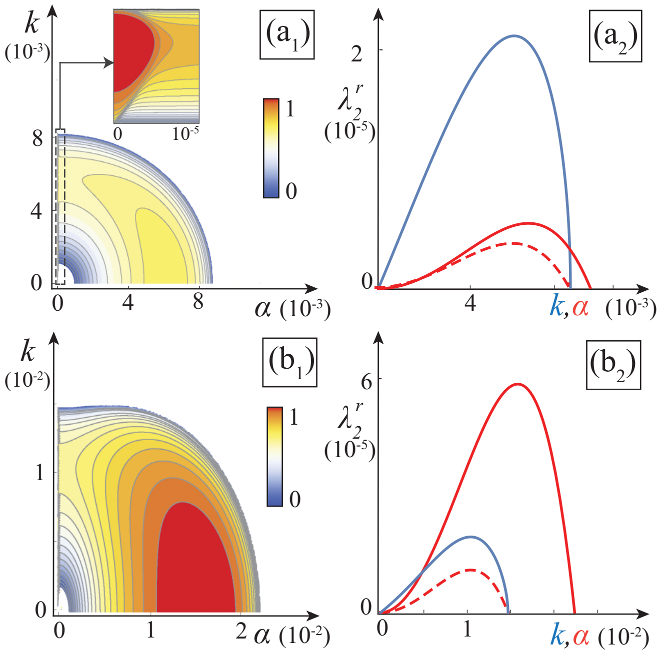

FIG. 2. Analysis of the growth rate λ_2^r from the 2D dispersion relation (ice case and $\theta = \pi/2 + \pi/9$). (a$_1$) Normalized contour plot of λ_2^r for $R = 0.1$. The maximum lays on the k axis, therefore flutings develop. (a$_2$) Comparison of λ_2^r on the k and α axes. (b$_1$) Normalized contour plot of λ_2^r for $R = 0.6$. The maximum lays on the α axis, therefore ripples develop. (b$_2$) Comparison of λ_2^r on the k and α axes. The red dotted line is the solution under the Stokes approximation, that is not adequate to reveal the ripple regime.

is associated with a spanwise perturbation. Therefore, we can introduce a normal mode ansatz with only transversal dependency

$$(h,\eta) = (1, V_{I,K}) + \zeta e^{ikz+\omega t}(H,\Lambda), \qquad (48)$$

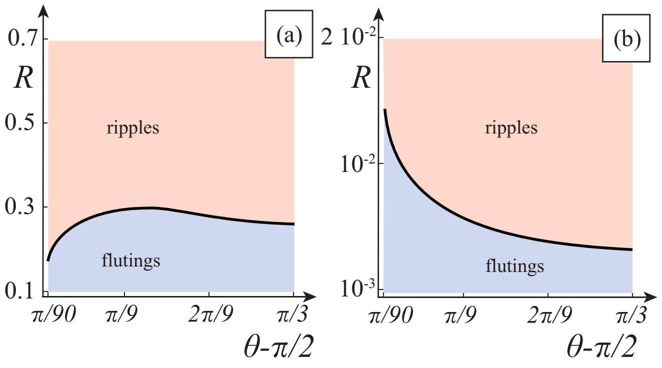

FIG. 3. Transition Reynolds number discriminating fluting and ripple regimes. Ice case (a) and karst case (b).

where the notation for the time dependency has been switched to ω to discriminate from the eigenvalues λ of Sec. III A. Hence, the real part of ω determines the growth rate, while its imaginary part stays for the angular phase. By substituting Eq. (48) into Eqs. (21) and (42) and linearizing, we obtain

$$\begin{pmatrix} \beta+\omega & \beta \\ -\frac{1}{\gamma} & a_{I,K} \end{pmatrix} \cdot \begin{pmatrix} H \\ \Lambda \end{pmatrix} = 0, \qquad (49)$$

where $\beta = k^2(\mathcal{C}k^2 + \delta)/3$, $a_I = \omega + 1/(r\gamma)$ and $a_K = \omega$. After imposing the determinant of the matrix equal to zero, the dispersion relations are obtained,

$$(\beta + \omega)\left(\omega + \frac{1}{r\gamma}\right) + \frac{\beta}{\gamma} = 0, \quad (I) \qquad (50a)$$

$$\beta(\gamma\omega + 1) + \omega^2\gamma = 0, \quad (K) \qquad (50b)$$

whose solutions, corresponding to the eigenvalues of the algebraic linear system Eq. (49), are

$$(\omega_{1,2})_I = -\left(\frac{\beta}{2} + \frac{1}{2r\gamma}\right)\left(1 \pm \sqrt{1 - \frac{4r\gamma\beta(r+1)}{(r\gamma\beta+1)^2}}\right), \qquad (51a)$$

$$(\omega_{1,2})_K = -\frac{\beta}{2}\left(1 \pm \sqrt{1 - \frac{4}{\gamma\beta}}\right). \qquad (51b)$$

The eigenvalues Eqs. (51) are real in the domain of instability, therefore flutings do not laterally migrate, and they become complex conjugate in the domain of stability, i.e., there is not a preferential direction for the decay of the perturbation. This is a consequence of the transversal invariance of the problem and it shows that the above mathematical setting is well-posed. Referring to ω_2 as the eigenvalues with the minus in front of the square root, it can be shown that ω_2 is always negative, while there is a range of wave numbers $k = [0, \sqrt{-\delta/\mathcal{C}}]$, where ω_1 is positive and flutings develop. In Fig. 4(a), it is reported an example of the behavior of the unstable eigenvalue versus the wave number, which corresponds to the type II$_s$ instability of the classification suggested by Ref. [39]. Interestingly, although the analytical relations for ω_1 are different in the two environments, the cutoff wave number remains the same. This is due to the fact that the dynamics is driven by the water film, that acts similarly in both cases. Analogously, the selected wave number, which corresponds to the least stable mode, i.e., the value k_1 such that $\omega_1'(k_1) = 0$, reads $k_1 = \sqrt{-\delta/2\mathcal{C}}$ for both environments. By recalling Eqs. (1) and (47), the corresponding dimensional wavelength reads

$$\hat{L}_z = \frac{2\pi\hat{h}_0}{k_1} = \pi\hat{l}_c\sqrt{-8\sec\theta}, \qquad (52)$$

where $\hat{l}_c = \sqrt{\sigma/\rho g}$ is the capillary length (recall that $\theta > \pi/2$). This result is quite peculiar because it shows that $\hat{L}_z$ does not depend on the hydrodynamics (Q), but only on the fluid properties (ρ,σ) and the geometry (θ). In Fig. 4(b) the behavior of $\hat{L}_z$ versus the slope is reported.

Due to Eq. (47), the two control parameters for the growth rate ω_1 are: θ and R. When R is kept constant, by setting $\omega_1 = 0$, the neutral stability curves in the (k,θ) plane are obtained, thus separating the stable from unstable domain, as reported in Fig. 4(c). The curves show that flutings develop when $\theta > \pi/2$ (so-called *inverted condition*). On the other hand, when θ is fixed at a particular value larger than $\pi/2$ and R is variable, the neutral stability curves in the parameter plane (k,R) start from the origin [Fig. 4(d)], that is all Reynolds number are unstable.

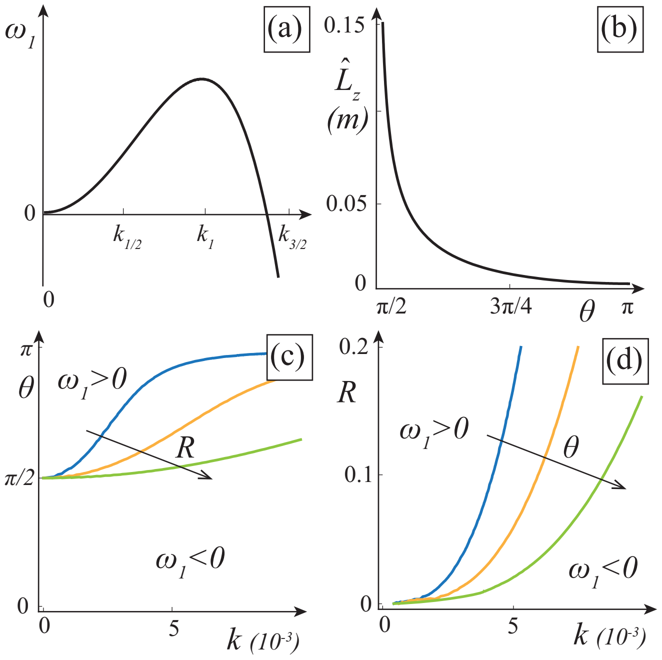

FIG. 4. Results of the linear stability analysis. (a) Typical behavior of the eigenvalue ω_1 versus the wave number k. (b) Dimensional wavelength of flutings versus the angle with the horizontal θ. (c) Neutral stability curves for the ice case with θ as control parameter ($R = 10^{-1}, 10^{-2}, 10^{-3}$). The instability is triggered at inverted conditions ($\theta > \pi/2$). (d) Neutral stability curves for the ice case with R as control parameter ($\theta - \pi/2 = \pi/36, \pi/18, \pi/9$). The plots for the karst case are qualitatively similar, with R spanning between 10^{-4} and 10^{-6}.

The present results agree with the outcomes of the theory developed in Ref. [11], where a y-dependent differential eigenvalue problem was solved with the aid of the Stokes approximation. The present approach of the gradient expansion circumvents the Stokes approximation and it is more suitable for further weakly nonlinear analyses, since the equation are provided in a one-dimensional form, where the y-dependence has been explicitly solved [see Eqs. (13)–(16) and Appendix A].

IV. NONLINEAR ANALYSIS

In this section, a weakly nonlinear analysis is performed through the technique of the center-unstable manifold projection. The aim is to provide an analytical solution for the finite amplitude of the fundamental mode. However, it is well known that solving the amplitude equation for the fundamental mode is sometimes not sufficient. In fact, when nonlinearities are in play, the linear modes are not any longer decoupled, hence finite-amplitude monochromatic waves may be destabilized by nonlinear interactions with other modes satisfying the so-called resonance condition [40]. In the case of quadratic nonlinearities, this condition reads: $k_l \pm k_p = k_m$, where k_m refers to the mode whose dynamic is in question and k_l and k_p are all possible modes that contribute to the dynamics of k_m. Although the fundamental k_m could be potentially unstable to any wavenumber (i.e., infinite combination of k_l and k_p), it is far simpler to derive stability criteria for disturbances of specific wavenumbers, if these disturbances are observed to be the dominant ones from physical observations. Concerning non-inverted falling films, experimental and theoretical works [25–27] have shown that, depending on the frequency of the fundamental, a subharmonic or a sideband instability is triggered. Moreover, previous analyses on open-flow systems, with long-wave instabilities as ours [28–30], have found instability to subharmonic disturbances. However, we point out that differently from these last works, in our system the modulation is not in the direction of the driving force, but it is transversal to it; see Sec. III B. Definitely, it can be noticed that in our system the range of unstable wave numbers spans from zero to $\sqrt{-\delta/\mathcal{C}}$; see Fig. 4(a). Hence, the 1/2 subharmonic of any wave within this range is linearly unstable, including the subharmonic of the fundamental, i.e., $k = k_1$, while the 3/2 subharmonic of the fundamental is stable. We will prove that, although the subharmonic of the fundamental is linearly unstable, the rising effect of the nonlinearities may allow the fundamental to saturate and the subharmonic to decay.

A. Center-unstable manifold projection

Weakly nonlinear theories in morphodynamics are usually developed with the aid of multiple-scale methods [41–43]. These techniques need the existence of a minimum in the neutral stability curve to be applied. As one can observe from Figs. 4(c) and 4(d), this in not the case, therefore we adopt a different approach, namely the center-unstable manifold projection. This choice is not only a novelty in the context of morphodynamics, but also a step forward with respect to the standard multiple-scale perturbation. In fact, it offers the advantage to find an amplitude solution valid not only in a neighbourhood of the critical point, but in any condition close to neutrality [40]. The center-unstable manifold projection does not stipulate that the unstable modes are nearly neutral, the only stipulation is that their amplitudes are small. This approach is sometimes known as the invariant manifold expansion [44], since the growth rates of the unstable modes are not expanded near the point where they vanish exactly at the neutral curve. Considering second order nonlinearities, system Eqs. (21)–(42) can be written as

$$\mathbf{u}_t = \mathbf{L}\mathbf{u} + \zeta\mathbf{N}(\mathbf{u}) + o(\zeta^2), \tag{53}$$

where $\mathbf{u} = (h,\eta)$, $\mathbf{L}$ is the differential operator associated with the linear system and $\mathbf{N}(\mathbf{u})$ contains all second order non-linearities. The linear eigenvalue problem associated with Eq. (53) states

$$\mathbf{L}\mathbf{w}_j = \omega_j \mathbf{w}_j, \tag{54}$$

where ω_j are the two eigenvalues reported in Eq. (51) and $\mathbf{w}_j$ are the correspondent eigenfunctions. The system is invariant to translation in z, therefore the linear problem may be Fourier transformed as follows:

$$\mathbf{w}_j(z) = \mathbf{v}_j(k)e^{ikz}. \tag{55}$$

Substituting Eq. (55) into Eq. (54) yields the projected eigenvalue problem,

$$L(k)\mathbf{v}_j(k) = \omega_j(k)\mathbf{v}_j(k), \tag{56}$$

where $L(k)$ is the same matrix appearing in Eq. (49). The corresponding adjoint eigenvalue problem reads

$$L^{\dagger}\mathbf{v}_j^{\dagger} = \omega_j^{*}\mathbf{v}_j^{\dagger}, \tag{57}$$

where star * refers to complex conjugate, while the symbol † stays for the adjoint (the dependence on k has been considered implicitly). We remind that $L^{\dagger}$ is defined by $(L\,\mathbf{x})\cdot\mathbf{y}^{*} = \mathbf{x}\cdot(L^{\dagger}\mathbf{y})^{*}$ and, because L has only real elements, its adjoint is simply the transpose, i.e., $L^{\dagger} = L^{T}$. After proper normalization, the eigenvectors $\mathbf{v}_i$ and the adjoint eigenvectors $\mathbf{v}^{\dagger}$ are orthonormal with respect to the dot product,

$$\mathbf{v}_i\cdot\mathbf{v}_j^{\dagger} = \delta_{ij}. \tag{58}$$

The fundamental mode $\omega_1(k)$ and its subharmonic $\omega_1(k/2)$ are the only possible unstable modes, while all other subharmonic or superharmonic modes are stable. The variables can now be expanded in terms of the eigenfunctions $\mathbf{w}_j$ given by Eq. (55),

$$\mathbf{u}(z,t) = \sum_{p=-\infty}^{+\infty}\sum_{j=1}^{2} A_{[j,\frac{p}{2}]}(t)\,\mathbf{v}_j\left(\frac{pk}{2}\right)\exp\left(\frac{ipkz}{2}\right), \tag{59}$$

where j and p are integer numbers and $A_{[j,\frac{p}{2}]}$ is the $p/2$ subharmonic associated with the eigenvalue j (we point out that Eq. (59) also takes into account the complex conjugate amplitudes as $A^{*}_{[j,\frac{p}{2}]} = A_{[j,-\frac{p}{2}]}$). Substituting Eq. (59) into Eq. (53), taking the dot product with the adjoint eigenfunctions and collecting the terms of the same Fourier modes, yields the equations for the two unstable modes,

$$\begin{aligned}\dot{A}_1 ={}& \omega_1(k)A_1 + P_1A_{\frac12}^2 + P_2^{(1)}A_{\frac12}A_{[2,\frac12]} + P_2A^{*}_{\frac12}A_{[1,\frac32]}\\ &+ P_2^{(2)}A^{*}_{[2,\frac12]}A_{[1,\frac32]} + P_2^{(3)}A^{*}_{\frac12}A_{[2,\frac32]} + \sum_{j=1}^{2}P_j^{(4)}A_1^{*}A_{[j,2]},\end{aligned} \tag{60a}$$

$$\begin{aligned}\dot{A}_{\frac12} ={}& \omega_1(k/2)\,A_{\frac12} + P_3A^{*}_{\frac12}A_1 + P_2^{(6)}A^{*}_{[2,\frac12]}A_1\\ &+ P_2^{(7)}A^{*}_{\frac12}A_{[2,1]} + P_4A_1^{*}A_{[1,\frac32]} + P_2^{(8)}A^{*}_{[2,1]}A_{[1,\frac32]}\\ &+ P_2^{(9)}A_1^{*}A_{[2,\frac32]} + \sum_{j=1}^{2}P_j^{(10)}A^{*}_{[1,\frac32]}A_{[j,2]},\end{aligned} \tag{60b}$$

where we have posed $A_{1,1} = A_1$ and $A_{1,\frac12} = A_{\frac12}$. Instead, the corresponding amplitude equations for the stable modes read

$$\dot{A}_{[2,\frac12]} = \omega_2(k/2)A_{[2,\frac12]} + Q_2^{(1)}A^{*}_{\frac12}A_1 + \cdots, \tag{61a}$$

$$\dot{A}_{[2,1]} = \omega_2(k/2)A_{[2,1]} + Q_2^{(3)}A_{\frac12}^2 + \cdots, \tag{61b}$$

$$\dot{A}_{[j,\frac32]} = \omega_j(3k/2)A_{[j,\frac32]} + Q_j^{(5)}A_{\frac12}A_1 + \cdots, \tag{61c}$$

$$\dot{A}_{[j,2]} = \omega_j(2k)A_{[j,2]} + Q_j^{(6)}A_1^2 + \cdots. \tag{61d}$$

Equations (60) and (61) represent a Galerkin-type projection of the full equations truncated at the second order non-linearities. Dots in the right-hand side of Eq. (61) refer to omitted quadratic terms involving interactions of the stable modes, while the derivation of all coefficients appearing in the present analysis, e.g., $P_j^{(m)}$ and $Q_i^{(n)}$ from Eqs. (60) and (61), is reported in the Appendix C and follow the nomenclature introduced by Ref. [45].

At this point, the center-unstable manifold theory allows the amplitudes of the stable modes to be projected onto the unstable ones, so that any $A_{[m,p]}$ in Eq. (61) is recast as a nonlinear combination of the neutral modes $A_1, A_{1/2}$ and their complex conjugate to $O(2)$. The procedure has been introduced by Ref. [40] but without details, which are outlined in the following for the sake of clarity. Let us consider, for instance, the stable mode $A_{[2,\frac12]} = F(A_1, A_{\frac12}, A_1^{*}, A^{*}_{\frac12})$, where F represents an approximation of the unstable invariant manifold and it is defined as a power series expansions to $O(2)$ of A_1 and $A_{\frac12}$ with unknown coefficients, namely

$$\begin{aligned}F ={}& aA_1^2 + bA_{\frac12}^2 + cA_1^{*2} + dA_{\frac12}^{*2} + eA_{\frac12}A_1\\ &+ fA^{*}_{\frac12}A_1 + gA_{\frac12}A_1^{*} + hA^{*}_{\frac12}A_1^{*}.\end{aligned} \tag{62}$$

Hence, the temporal derivative of the stable modes $A_{[2,\frac12]}$ reads

$$\dot{A}_{[2,\frac12]} = \frac{\partial F}{\partial A_1}\dot{A}_1 + \frac{\partial F}{\partial A_{\frac12}}\dot{A}_{\frac12} + \frac{\partial F}{\partial A_1^{*}}\dot{A}_1^{*} + \frac{\partial F}{\partial A^{*}_{\frac12}}\dot{A}^{*}_{\frac12}. \tag{63}$$

Substituting Eqs. (60)–(61a) and (62) in Eq. (63), keeping only leading order terms and collecting like powers of A_1, $A_{\frac12}, A_1^{*}, A^{*}_{\frac12}$ yields

$$\begin{aligned}&a[2\omega_1(k) - \omega_2(k/2)]A_1^2 + b\,\omega_2(k/2)A_{\frac12}^2 + g\,\omega_1^{*}(k)A_1^{*}A_{\frac12}\\ &+ c[2\omega_1^{*}(k) - \omega_2(k/2)]A_1^{*2} + d[2\omega_1^{*}(k/2) - \omega_2(k/2)]A_{\frac12}^{*2}\\ &+ e\,\omega_1(k)A_1A_{\frac12} + h[\omega_1^{*}(k) + \omega_1^{*}(k/2) - \omega_2(k/2)]A_1^{*}A^{*}_{\frac12}\\ &+ \big\{-Q_2^{(1)} + f[\omega_1^{*}(k/2) + \omega_1(k) - \omega_2(k/2)]\big\}A_1A^{*}_{\frac12} = 0.\end{aligned} \tag{64}$$

A solution to Eq. (64) is made by imposing all null coefficients except f, which reads

$$f = -\frac{Q_2^{(1)}}{\omega_2(k/2) - \omega_1(k/2) - \omega_1(k)} = R_2^{(1)}, \tag{65}$$

reminding that $\omega_1^{*} = \omega_1$. Repeating the same procedure for every stable amplitude of interest yields

$$\begin{aligned}&A_{[2,\frac12]} \sim R_2^{(1)}A^{*}_{\frac12}A_1, \quad A_{[2,1]} \sim R_2^{(3)}A_{\frac12}^2,\\ &A_{[j,\frac32]} \sim R_j^{(5)}A_{\frac12}A_1, \quad A_{[j,2]} \sim R_j^{(6)}A_1^2.\end{aligned} \tag{66}$$

After substituting Eq. (66) into Eq. (60), the ultimate master amplitude equations for 1/2 subharmonic instabilities of quadratic systems with translational invariance in z and t are obtained,

$$\dot{A}_1 = \omega_1A_1 + P_1A_{\frac12}^2 + \tilde{D}_2|A_{\frac12}|^2A_1 + D_1|A_1|^2A_1, \tag{67}$$

$$\dot{A}_{\frac12} = \omega_{\frac12}A_{\frac12} + P_3A_{\frac12}A_1 + \tilde{D}_5|A_1|^2A_{\frac12} + D_6|A_{\frac12}|^2A_{\frac12}, \tag{68}$$

where $\omega_1 = \omega_1(k)$ and $\omega_{\frac12} = \omega_1(k/2)$.

B. Stuart-Landau equation

The Stuart-Landau equation describes the dynamic of the fundamental without considering the influences of the other potentially destabilizing modes. Therefore, it is readily obtained by neglecting the terms involving $A_{\frac{1}{2}}$ in Eq. (67),

$$\dot{A}_1 = (\omega_1 + D_1|A_1|^2)A_1, \tag{69}$$

where both coefficients ω_1 and D_1 are real in the domain of instability, i.e., flutings do not laterally migrate. The fixed point of Eq. (69) is obtained by setting $\dot{A}_1 = 0$, that gives, besides the trivial solution, the finite saturated amplitude,

$$|A_s|_I^2 = -\left(\frac{\omega_1}{D_1}\right)_I = \frac{2r^2\Sigma_I(\beta\gamma r + 1)}{9[\beta^3\gamma^3r^3(\Sigma_I + 1) - \beta^2\gamma^2r^2(r+1)(\Sigma_I + 3) - \beta\gamma r(r+1)(\Sigma_I - 3) + \Sigma_I - 1]}, \tag{70a}$$

$$|A_s|_K^2 = -\left(\frac{\omega_1}{D_1}\right)_K = \frac{4(\gamma\beta - 4)}{27\gamma^2\beta^2\Sigma_K(1 + \Sigma_K)[-2 + \beta\gamma(1 + \Sigma_K)]}, \tag{70b}$$

where $\Sigma_I = \sqrt{1 - 4\beta\gamma r(r+1)/(\beta\gamma r + 1)^2}$ and $\Sigma_K = \sqrt{1 - 4/\beta\gamma}$. To dimensionally reconstruct the variables $\hat{h}$ and $\hat{\eta}$, one should use Eq. (59) and the uniform flow depth $\hat{h}_0$. As we discuss in Sec. IV D, wherein numerical simulations of the original Eqs. (21) and (42) are showed, the solutions Eqs. (70) lead to accurate predictions for the flow depth $\hat{h}$, but not for the bottom height $\hat{\eta}$. However, the direct use of the wall evolution Eq. (42) allows us to bypass this drawback. Similar considerations regard the so-called saturation time $\hat{t}_s$, defined here so that $A_1(0) = 0.001A_s$ and $A_1(t_s) = 0.99A_s$.

C. Subharmonic stability analysis

To study the stability of the saturated fundamental to disturbances with 1/2 its wave number, we perturb the fundamental and its 1/2 subharmonic around the state $(A_s,0)$, respectively, as follows:

$$\left(A_1, A_{\frac{1}{2}}\right) = (A_s,0) + \psi\left(a_1, a_{\frac{1}{2}}\right). \tag{71}$$

Substituting Eq. (71) into the master Eqs. (67) and (68) and linearizing, yields

$$\dot{a}_1 = 2D_1A_s^2a_1, \tag{72}$$

$$\dot{a}_{\frac{1}{2}} = \left(\omega_{\frac{1}{2}} + \tilde{D}_5A_s^2 + P_3A_s\right)a_{\frac{1}{2}} = \tilde{\omega}_{\frac{1}{2}}a_{\frac{1}{2}}. \tag{73}$$

It can be noticed that, since the fundamental is unstable, i.e., $\omega_1 > 0$, Eq. (70) stipulates that D_1 must be negative for a saturated wave to exist. From Eq. (72), it is therefore obtained that the saturated monochromatic wave is always stable to disturbances of the same wave number. The instability may instead arise from Eq. (73), depending on the sign of the growth rate of the subharmonic corrected by nonlinearities, i.e., $\tilde{\omega}_{\frac{1}{2}}$. In both environments $\tilde{\omega}_{\frac{1}{2}}$ is negative in the domain of instability, that means that the fundamental is always stable to subharmonic disturbances. We have also tested numerically the previous conclusion by solving directly the Eqs. (67) and (68). The results of a representative simulation are reported in Fig. 5. Starting from a flat bottom, the fundamental A_1 (light blue line) and its subharmonic $A_{\frac{1}{2}}$ (red line) initially grow in agreement to the linear instability. Then, the influence of non-linearities become relevant, so that the fundamental saturates while its subharmonic decays to zero. This result is sufficient to prove the stability of the fundamental to 1/2 subharmonic when both modes are perturbed around the null state. Nevertheless, as the stability analysis Eq. (71) has been performed around the basic state $(A_1, A_{\frac{1}{2}}) = (A_s,0)$, we have also introduced a small perturbation when the fundamental is already saturated while the subharmonic is vanishing, see insets. It can be observed that both perturbations decrease in time, showing once more the stability of the saturated fundamental to its 1/2 subharmonic.

D. Numerical simulations of the system Eqs. (21)–(42)

The complete set of Eqs. (21), (42) has also been solved numerically for both environments. In Fig. 6(a) the wavy behavior of saturated $\hat{h}$ in space is reported for the ice case. The y axis has been reversed to remind the reader of the slightly overhanging conditions. The wavelength $\hat{L}_z$ corresponds exactly to the one expected by the linear theory; see Eq. (52). The amplitude is well predicted by the center manifold projection, see Eq. (70), especially for the lower limit of $\hat{h}$ (upper red line). Indeed, the amplitude of the fundamental can not catch the asymmetry of the solution, for which other harmonics and fully nonlinear effects should be included. Additionally, Fig. 6(b) shows the amplitude dynamics in time for a given spatial coordinate. Also in this case, the Stuart-Landau Eq. (69) offers a good approximation in evaluating the saturation time $\hat{t}_s$.

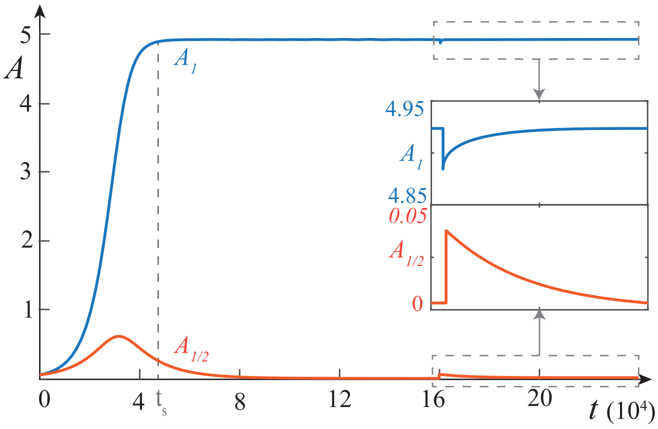

FIG. 5. Subharmonic stability. Numerical simulation of the nonlinear amplitude Eqs. (67) and (68) for A_1 (blue line) and $A_{\frac{1}{2}}$ (red line). The subharmonic mode 1/2 is initially linearly unstable, then it is stabilized by the nonlinear interactions with the fundamental that saturates. The insets show how perturbations of the basic state $(A_1, A_{\frac{1}{2}}) = (A_s,0)$ decrease in time, thus proving the stability of the fundamental. (Ice case, $R = 0.05$ and $\theta = \pi/2 + \pi/36$. Same qualitatively results hold for the karst case.)

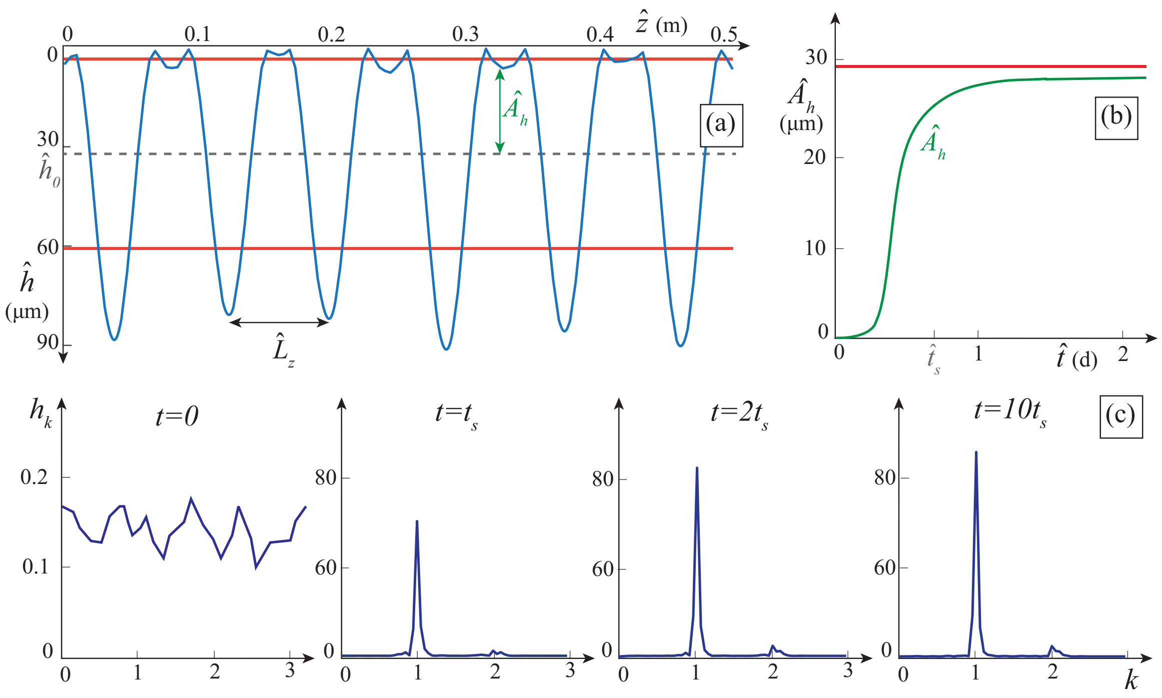

FIG. 6. Results of a numerical simulation (ice case, $R = 0.05$, $\theta = \pi/2 + \pi/36$). (a) Wavy spatial behavior of the saturated $\hat{h}$ (blue line). The initial condition is the uniform water depth $\hat{h}_0$ (gray dotted line). The red lines indicate the finite amplitude height expected by the nonlinear analytical theory. Both wavelength and amplitude ($\hat{L}_z$ and $\hat{A}_h$) are correctly predicted by the theory. (b) Evolution in time of water depth amplitude $\hat{A}_h$ for the case of panel *a* and $\hat{z} == 0.32$ m. The Stuart-Landau Eq. (69) fairly estimates the saturation time $\hat{t}_s$. (c) Evolution in time of the h spectrum starting from a white noise perturbation. The solutions converges to the fundamental and no nonlinear instabilities are detected.

Regarding the bottom height $\hat{\eta}$, the prediction of the linear analysis are robust, i.e., the wavelength $\hat{L}_z$ is consistent with the one of the water depth. However, the center manifold projection is not able to correctly capture the morphologic dynamics. This is likely due to the fact that the dynamics of η is mainly represented on the *stable* manifold of the $A_{[j,p]}$-phase space. This opens to two further separated remarks for the two different environments.

In the karst case, one can observe that the term $h - 1$ in Eq. (42b) is generally non-null, being the water depth wavy as in Fig. 6(a). As there are no terms related to η (linearly or nonlinearly) to counteract the linear growing, flutings grow endlessly. This could explain the very large amplitude of flutings in flowstone worldwide, see Fig. 7. Instead in the ice case, the linear term involving the perturbation of η in Eq. (42a) does stop the pattern growth. Thus, by repeating the ansatz as in the linear analysis ($\eta = V_I t + \eta_1$ and $h = 1 + h_1$), the r.h.s of Eq. (42a) vanishes when the bottom height reaches a saturated value, η_{1s}, equal to

$$\eta_{1s} = r h_{1s}. \tag{74}$$

As h_{1s} is correctly given by the center manifold approximation through Eq. (70), Eq. (74) provides a very satisfactory result of the height of the pattern. Using the dimensional set of parameter of Fig. 6 and reminding that $r = \hat{b}/\hat{h}_0$, one obtains $\hat{\eta}_1 \sim 0.47$m.

Finally, to test the stability of the fundamental to nonlinear disturbances of other modes, we have performed long-term numerical simulation for the Benney-like Eq. (21) with the bottom fixed. This latter choice is due to the fact that the dynamics of the whole system is driven by the water film. Figure 6(c) shows the temporal evolution of the spectrum. Starting from a random white noise with all harmonics excited, the solution converges to the saturation of the fastest growing mode, i.e., the fundamental. This mode is not consequently destabilized nor by the 1/2 subharmonic, in agreement with the prediction of Sec. IV C, nor by any other slow modes (higher order subharmonics at small wave numbers that act at long times).

V. DISCUSSION AND CONCLUSION

In the present work we have analyzed flutings formation, linearly and nonlinearly, through a unified approach which accounts for both the ice and the karst case. This task was addressed by combining two mathematical techniques used for the first time in the context of morphological patterns: gradient expansion and center-unstable manifold projection.

Through the technique of gradient expansion we have achieved Eq. (21), that is a Benney-type equation accounting for the evolution of the evolving solid substrate. The coupling of the latter with the evolution equation for the substrate Eq. (42), provides a parsimonious modeling of fluting dynamics. The outcomes of the linear analysis confirm the results previously obtained by more sophisticated models [e.g., [11]], but also provide further achievements. First, we have relaxed the Stokes approximation and solved the film flow

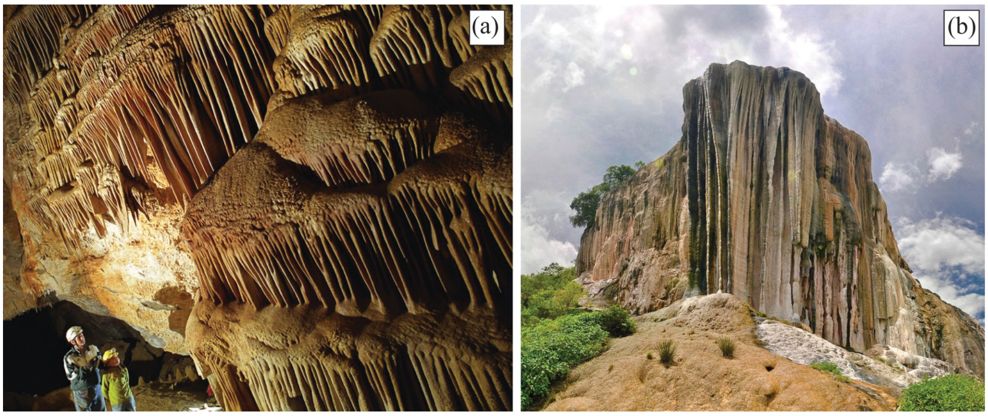

FIG. 7. Examples of very large amplitude karst flutings. (a) Yordas Cave, England. (b) *Hierve el Agua*, Mexico.

field without the necessity to solve y-dependent differential equations. Secondly, the gain in the analytical treatment of the linear stability analysis has favored the development of a nonlinear investigation.

Previous weakly nonlinear approaches have limited their validity close to the critical conditions [46]. The extension of the weakly nonlinear validity to the interior of the unstable domain has usually been conjectured since it was shown to be reasonable for some hydrodynamic instabilities [47]. Whether this conjecture is also valid for morphodynamic instabilities remains open. Instead, the technique of center manifold projection furnishes the Stuart-Landau equation valid for any condition *close* to the neutral curve and not only in a neighbourhood of the critical point [45].

The selected wave number Eq. (52) and the finite amplitude Eq. (70), given in a closed analytical form, provide the complete description of fluting system with respect to two control parameters: the Reynolds number and the angle with the horizontal. These quantitative results also have a value from a palaeoreconstructive point of view. In fact, speleothems, such as cave flutings, contain information on the past climate since they evolve with a timescale of millennia [2].

Nevertheless, defining quantitatively finite amplitude monochromatic waves may be not sufficient as they can be destabilized by nonlinear interactions with other modes. In particular, in other open flow systems with long-wave instabilities, the growth of subharmonic modes was detected. Therefore we have studied the linear stability of the finite-amplitude fundamental mode to $1/2$ subharmonic disturbances, verifying, both analytically and numerically, that flutings are stable to subharmonic disturbances as nonlinearities allow the fundamental mode to saturate and the subharmonic to decay. From a practical point view, this means that the predictions of the linear and nonlinear analysis are robust.

Eventually, the numerical simulations of the Eqs. (21)–(42) have confirmed most of the theoretical results. The linear theory is fully verified, while the nonlinear theory agrees correctly with the simulations for the hydrodynamics, but not for the morphodynamics. This is probably due to the fact that the center manifold projection looses some aspects of the dynamics of the stable manifold. Nevertheless, thanks to the correct prediction of the hydrodynamic behavior, one may reconstruct the morphodynamics directly from the steady solution of Eq. (42). This leads to the finite amplitude Eq. (74) for ice flutings and to nonsaturating patterns for the karst case.

An analysis not reported in the paper, regards the asymptotic stability of the system for $\theta < \pi/2$, i.e., with a wall not overhung. In fact, many dynamical systems are not completely described by the eigenvalues analysis as they perform relevant transient behaviours [48,49]. We have verified through a nonmodal study the absence of a transient behavior in the present context, giving reliability to the asymptotic eigenvalue stability.

Another issue that deserves further attention are the outcomes of the analysis close to verticality. In fact, when $\theta \rightarrow \pi/2^+$, the dimensional wavelength and the finite amplitude diverge to infinite [see Fig. 4(b)], that means that there is no wavelength selection nor amplitude saturation at this critical condition. This shortcoming could be remedied by a non-parallel stability theory, englobing the radius of curvature of the liquid-solid interface and non-parallelism of the flow field in a neighbourhood of the vertical tangent point [11].

Finally, the analytical nonlinear approach of the center manifold projection may be broaden to other spatially extended systems so to determine the saturation amplitude of the fundamental mode and its stability to disturbances of different wave numbers. A notable example is the pattern formation occurring in supraglacial drainage systems made up of evenly spaced channels [7]. This phenomena has been investigated only linearly and still awaits for a nonlinear analysis. Furthermore, the present approach could give relevant quantitative results even in the branch of morphodynamics that deals with river environments, where the coupling between sediment transport and flow dynamics triggers the formation of sand patterns on the watercourse bed; for a review see Ref. [50]. In this case, the hydraulic conditions differentiate noticeably the pattern dimensions. At low flows, it is common to find small corrugations of the bottom, called ripples, with typical wavelengths of centimetres and amplitudes of millimetres. For higher flows, asymmetric bedforms, named dunes, develop and their spatial scale is of the order of the flow depth; while an exceptionally high flow, such as during a flood event, triggers the formation of large scale bedforms, so-called bars, that scale with the channel width. All these patterns could benefit from the advantages of the present technique.

APPENDIX A: SOLUTIONS TO ORDER ϵ SYSTEM EQS. (17)–(20)

$$u_1 = \tfrac{1}{6}(y-\eta)(y-2h-\eta)\{3\delta(h+\eta)_x - 3\mathcal{C}[(h+\eta)_{xzz} + (h+\eta)_{zzz}] + Rhh_x[2h(\eta-y) - 4h^2 + (y-\eta)^2]\}, \tag{A1}$$

$$w_1 = \tfrac{1}{2}(y-\eta)(-2h-\eta+y)\{\delta(h+\eta)_z - \mathcal{C}[(h+\eta)_{zzz} + (h+\eta)_{xxz}]\}, \tag{A2}$$

$$v_1 = \int_\eta^y (u_{1,x} + w_{1,z})dy. \tag{A3}$$

We point out that the expression for p_1 is not reported as it is not needed to reach Eq. (21).

APPENDIX B: LINEAR MATRIX, DISPERSION RELATION, AND EIGENVALUES FOR THE 2D MODEL

The matrix associated with the linear system Eq. (45) depends on the environment considered. Its general form reads

$$\mathbf{L}_{I,K} = \begin{pmatrix} a_1 & a_2 \\ a_3 & a_4 \end{pmatrix}. \tag{B1}$$

In the ice case,

$$a_1 = 30i\alpha + 5K^2(\delta + K^2\mathcal{C}) - 8\alpha^2 R + 15\lambda, \quad a_3 = -r,$$
$$a_2 = 5K^2(K^2\mathcal{C} + \delta), \quad a_4 = 1 + r\gamma\omega,$$

and $K^2 = k^2 + \alpha^2$. Imposing the determinant equal to zero gives the dispersion relation

$$5K^2(r\gamma\lambda + r + 1)(K^2\mathcal{C} + \delta) + (1 + r\gamma\lambda)(30i\alpha - 8\alpha^2 R + 15\lambda) = 0, \tag{B2}$$

whose two complex conjugate solutions are the eigenvalues of the linear system

$$\lambda_{1,2} = \frac{1}{30r\gamma}(a \pm \sqrt{b}), \tag{B3}$$

with

$$a = -15 - 30i\alpha\gamma - 5K^2 r\gamma(\delta + K^2\mathcal{C}) + 8\gamma\alpha^2 R,$$
$$b = -60r\gamma[2\alpha(15i - 4R\alpha) + 5K^2(1+r)(K^2\mathcal{C} + \delta)] + [15 + 2r\alpha(15i - 4R\alpha)\gamma + 5K^2 r\gamma(K^2\mathcal{C} + \delta)]^2.$$

In the karst case, the first line of the matrix remains the same, while $a_3 = -1$ and $a_4 = \gamma\omega$. Imposing the determinant equal to zero gives the dispersion relation

$$5K^2(\gamma\lambda + 1)(K^2\mathcal{C} + \delta) + \gamma\lambda(30i\alpha - 8\alpha^2 R + 15\lambda) = 0, \tag{B4}$$

whose two complex conjugate solutions are the eigenvalues of the linear system

$$\lambda_{1,2} = \frac{1}{30\gamma}(a \pm \sqrt{b}), \tag{B5}$$

with

$$a = -30i\alpha - 5K^2(\delta + K^2\mathcal{C}) + 8\alpha^2 R,$$
$$b = \gamma\{-300K^2(\delta + K^2\mathcal{C}) + \gamma[5K^2(\delta + K^2\mathcal{C}) + 2\alpha(-4\alpha R + 15i)]^2\}.$$

APPENDIX C: NONLINEAR COEFFICIENTS

Following Ref. [45], we define a function G,

$$G(\alpha,\beta,\gamma,j,m,n) = \mathbf{N}[\mathbf{v}_m(\beta k)e^{i\beta kx}, \mathbf{v}_n(\gamma k)e^{i\gamma kx}] \cdot \hat{\mathbf{v}}_j(\alpha k)e^{-i\alpha kx}, \tag{C1}$$

where (α,β,γ) are the indices for the interacting Fourier modes that satisfy the resonant condition $\alpha = \beta + \gamma$, and (j,m,n) stay for the eigenmodes. Let us consider two generic vectors $\mathbf{u} = (u_1,u_2)$ and $\mathbf{v} = (v_1,v_2)$, $\mathbf{N}[\mathbf{u},\mathbf{w}] = (N_1,N_2)$ is the symmetric function containing all second order nonlinearities of system Eq. (53):

$$\begin{aligned} N_1 = {} & \tfrac{1}{2}\{u_{1,z}[\delta(v_1 + v_2)_z - \mathcal{C}(v_1 + v_2)_{zzz}] + u_1[\delta(v_1 + v_2)_{zz} - \mathcal{C}(v_1 + v_2)_{zzzz}]\} \\ & + \tfrac{1}{2}\{v_{1,z}[\delta(u_1 + u_2)_z - \mathcal{C}(u_1 + u_2)_{zzz}] + v_1[\delta(u_1 + u_2)_{zz} - \mathcal{C}(u_1 + u_2)_{zzzz}]\}, \end{aligned} \tag{C2}$$

and $N_2 = 0$. The interaction coefficients in Eqs. (60) and (61) are

$$\begin{aligned}
P_1 &= G[1,1/2,1/2,1,1,1], \quad P_2 = 2G[1,-1/2,3/2,1,1,1],\\
P_3 &= 2G[1/2,-1/2,1,1,1,1], \quad P_4 = 2G[1/2,-1,3/2,1,1,1],\\
P_j^{(1)} &= G[1,1/2,1/2,1,j,1], \quad P_j^{(2)} = 2G[1,-1/2,3/2,1,j,1],\\
P_j^{(3)} &= 2G[1,-1/2,3/2,1,1,j], \quad P_j^{(4)} = 2G[1,-1,2,1,1,j],\\
P_j^{(5)} &= 2G[1,-3/2,5/2,1,1,j], \quad P_j^{(6)} = 2G[1/2,-1/2,1,1,j,1],\\
P_j^{(7)} &= 2G[1/2,-1/2,1,1,1,j], \quad P_j^{(8)} = 2G[1/2,-1,3/2,1,j,1],\\
P_j^{(9)} &= 2G[1/2,-1,3/2,1,1,j], \quad P_j^{(10)} = 2G[1/2,-3/2,2,1,1,j],\\
Q_j^{(1)} &= 2G[1/2,-1/2,1,j,1,1], \quad Q_j^{(3)} = G[1,1/2,1/2,j,1,1],\\
Q_j^{(5)} &= 2G[3/2,1/2,1,j,1,1], \quad Q_j^{(6)} = G[2,1,1,j,1,1].
\end{aligned}$$

After defining the function H,

$$H(Q,\alpha,m,n) = -Q/[\omega_j(\alpha k) - \omega_1(mk) - \omega_1(nk)], \tag{C3}$$

the coefficients of the center-unstable manifold projection Eq. (66) read

$$\begin{aligned}
R_j^{(1)} &= H\big[Q_j^{(1)},1/2,-1/2,1\big], \quad R_j^{(3)} = H\big[Q_j^{(3)},1,1/2,1/2\big],\\
R_j^{(5)} &= H\big[Q_j^{(5)},3/2,1/2,1\big], \quad R_j^{(6)} = H\big[Q_j^{(6)},2,1,1\big].
\end{aligned}$$

The coefficients of the projected Eqs. (67) and (68) are

$$\begin{aligned}
D_1 &= P_1^4 R_1^{(6)} + P_2^4 R_2^{(6)}, \quad D_2 = P_2^{(1)} R_2^{(1)} + P_2^{(3)} R_2^{(5)},\\
D_5 &= P_2^{(6)} R_2^{(1)} + P_2^{(9)} R_2^{(5)}, \quad D_6 = P_2^{(7)} R_2^{(3)},\\
\tilde{D}_2 &= D_2 - P_2 P_5/(\omega_{3/2} - \omega_{1/2} - \omega_1), \quad \tilde{D}_5 = D_5 - P_4 P_5/(\omega_{3/2} - \omega_{1/2} - \omega_1).
\end{aligned}$$

---

[1] P. Meakin and B. Jamtveit, Proc. R. Soc. A 20090189 (2009).

[2] I. J. Fairchild *et al.*, Earth-Sci. Rev. **75**, 105 (2006).

[3] M. B. Short, J. C. Baygents, and R. E. Goldstein, Phys. Fluids **17**, 083101 (2005).

[4] C. Camporeale and L. Ridolfi, Phys. Rev. Lett. **108**, 238501 (2012).

[5] C. Camporeale and L. Ridolfi, J. Fluid. Mech. **694**, 225 (2012).

[6] M. Yokokawa, N. Izumi, K. Naito, G. Parker, T. Yamada, and R. Greve, J. Geophys. Res. Earth Surf. **121**, 1023 (2016).

[7] E. Mantelli, C. Camporeale, and L. Ridolfi, Water Resour. Res. **51**, 7044 (2015).

[8] K. Ueno, Phys. Fluids **19**, 093602 (2007).

[9] K. Ueno, M. Farzaneh, S. Yamaguchi, and H. Tsuji, Fluid. Dynam. Res. **42**, 025508 (2009).

[10] A. Chen and S. Morris, New J. Phys. **15**, 103012 (2013).

[11] C. Camporeale, J. Fluid. Mech. **778**, 89 (2015).

[12] D. J. Benney, Stud. Appl. Math. **45**, 150 (1966).

[13] P. Rosenau, A. Oron, and J. Hyman, Phys. Fluids A-Fluid **4**, 1102 (1992).

[14] L. A. Dávalos-Orozco, S. H. Davis, and S. G. Bankoff, Phys. Rev. E **55**, 374 (1997).

[15] S. Joo, S. Davis, and S. Bankoff, Phys. Fluids A-Fluid **3**, 231 (1991).

[16] C. Ruyer-Quil and P. Manneville, Eur. Phys. J. B **6**, 277 (1998).

[17] C. Ruyer-Quil and P. Manneville, Eur. Phys. J. B **15**, 357 (2000).

[18] G. Sivashinsky and D. Michelson, Prog. Theor. Phys. **63**, 2112 (1980).

[19] A. Oron and P. Rosenau, Phys. Fluids A-Fluid **1**, 1155 (1989).

[20] J. Hyman, B. Nicolaenko, and S. Zaleski, Physica D **23**, 265 (1986).

[21] O. K. Matar and S. Kumar, J. Eng. Math. **57**, 145 (2007).

[22] O. K. Matar, R. V. Craster, and S. Kumar, Phys. Rev. E **76**, 056301 (2007).

[23] J. Warren, W. Boettinger, and A. Roosen, Acta Mater. **46**, 3247 (1998).

[24] J. Hunter, Z. Li, and H. Zhao, J. Comput. Phys. **183**, 335 (2002).

[25] J. Liu and J. P. Gollub, Phys. Rev. Lett. **70**, 2289 (1993).

[26] N. Brauner and D. Maron, Int. J. Heat Mass Tran. **25**, 99 (1982).

[27] M. Cheng and H. Chang, Phys. Fluids **7**, 34 (1995).

[28] R. Kelly, J. Fluid Mech. **27**, 657 (1967).

[29] P. A. Monkewitz, J. Fluid. Mech. **188**, 223 (1988).

[30] T. Prokopiou, M. Cheng, and H. Chang, J. Fluid Mech. **222**, 665 (1991).

[31] W. Nusselt, Zetrschr. Ver. Deutch. Ing. **60**, 541 (1916).

[32] S. Kalliadasis, C. Ruyer-Quil, B. Scheid, and M. G. Velarde, *Falling Liquid Films* (Springer Science & Business Media, Berlin, 2011), Vol. 176.

[33] R. Craster and O. Matar, Rev. Mod. Phys. **81**, 1131 (2009).

[34] C. Camporeale, J. Fluid Mech. **826**, 636 (2017).

[35] B. Gjevik, Phys. Fluids **13**, 1918 (1970).

[36] C. Camporeale, R. Vesipa, and L. Ridolfi, Phys. Rev. Fluids **2**, 053904 (2017).

[37] D. Romanov, G. Kaufmann, and W. Dreybrodt, Geochim. Cosmochim. Acta **72**, 423 (2008).

[38] T.-S. Lin and L. Kondic, Phys. Fluids **22**, 052105 (2010).

[39] M. Cross and P. Hohenberg, Rev. Mod. Phys. **65**, 851 (1993).

[40] M. Cheng and H. Chang, Phys. Fluids A F. (1989-1993) **2**, 1364 (1990).

[41] G. Vittori and P. Blondeaux, J. Fluid. Mech. **218**, 19 (1990).

[42] G. Seminara and M. Tubino, J. Fluid. Mech. **244**, 257 (1992).

[43] M. Colombini, G. Seminara, and M. Tubino, J. Fluid. Mech. **181**, 213 (1987).

[44] A. Roberts, SIAM J. Math. Anal. **20**, 1447 (1989).

[45] M. Cheng and H. Chang, Phys. Fluids A F **4**, 505 (1992).

[46] K. Stewartson and J. Stuart, J. Fluid Mech. **48**, 529 (1971).

[47] C. Godrèche, P. Manneville, and B. Castaing, *Hydrodynamics and Nonlinear Instabilities* (Cambridge University Press, Cambridge, 2005), Vol. 3.

[48] T. Biancalani, F. Jafarpour, and N. Goldenfeld, Phys. Rev. Lett. **118**, 018101 (2017).

[49] A. Caruso, R. Vesipa, C. Camporeale, L. Ridolfi, and P. J. Schmid, Phys. Rev. E **93**, 053110 (2016).

[50] G. Seminara, Annu. Rev. Fluid Mech. **42**, 43 (2010).